07,01

Structural changes in ferromagnetic microwires (PrDy)(FeCo)B under vacuum annealing

© E.V. Dvoretskaya, R.B. Morgunov

Federal Research Center of Problems of Chemical Physics and Medicinal Chemistry RAS, Chernogolovka, Russia

E-mail: Dvoretskaya95@yandex.ru

Received October 7, 2024
Revised November 7, 2024
Accepted November 9, 2024

Vacuum annealing of amorphous (PrDy)(FeCo)B microwires causes a redistribution of chemical elements in areas with different types of crystal lattice. The bulk of the annealed microwire has a tetragonal structure and corresponds to the alloy $(PrDy)_2(FeCo)_{14}B$. Nonequilibrium inclusions with a body-centered cubic lattice (BCC) are formed in the annealed microwire. These inclusions have an excess of Fe and Co and a depletion of rare earth elements Dy and Pr compared to the material of the surrounding tetragonal lattice. Thermal adjustment of the chemical, phase and structural composition of the microwires allows obtaining nonequilibrium states of the alloy with modified magnetic properties.

Keywords: microstructures, phase composition, heat treatment, phase inclusions.

DOI: 10.61011/PSS.2024.11.60104.256

1. Introduction

Alloys of *RE-TM*-B family (*RE* — rare earth metal, *TM* — transition metal, B — boron), such as NdFeB [1–5], are the backbone of the magnet industry. Chemical modification of *RE* and *TM* sublattices by replacing metal atoms provides the desired properties of these solid magnets. The conditions of phase formation are very different from those in bulk alloys *RE-TM*-B in microstructures. Exotic magnetic states can be achieved in microstructures for this reason.

The active study of the electrical and magnetic properties of multicomponent ferromagnetic microwires has been driven recently by the expansion of their field of application as devices for non-volatile magnetic memory [6,7]. Magnetic tweezers and micromanipulators based on *RE-TM*-B alloys are proposed [8,9]. A strong change of magnetic impedance (MI) was found in $Co_{27.4}Fe_5B_{12.26}Si_{12.26}Ni_{43.08}$ and $Co_{64.82}Fe_{3.9}B_{10.2}Si_{12}Cr_9Mo_{0.08}$ microwires [10] (140−300%) with temperature variations, which makes it possible to use such microwires as miniature temperature sensors. Since stable temperature characteristics are required to use the MI effect in sensors and transmitters [10–12], the possibility of modifying the magnetic properties of FeSiBCuNb and FeSiB microwires by local surface crystallization by heat treatment and chemical etching is considered in [13]. Domains with radial magnetization, periodically alternating along a ferromagnetic microwire are reported in [14]. A similar domain structure was found in (PrDy)(FeCo)B microwires [15]. However, the conditions for the formation of a periodic magnetic structure are not completely clear, although it has been established that the formation of radial domains depends on the phase composition and distribution of chemical elements in the microwire. Thus, an explanation of the formation of the magnetic properties of microstructures requires knowledge of the chemical and phase composition features. There are many factors in microwires that change the phase formation in them. The initial amorphous state of the microwires is highly nonequilibrium. Initialization of relaxation of this state by annealing results in the passage of the system through multiple intermediate metastable or labile states that are not found in bulk materials.

The purpose of this paper was to determine the stoichiometric deviations and the presence of various phases in an amorphous ferromagnetic microwire (PrDy)(FeCo)B, as well as to establish patterns of formation and transformation of phases as a result of a microwire thermal annealing.

2. Samples and experimental methods

$Pr_{3.5}Dy_6Fe_{49}Co_{40}B_{2.5}$ amorphous microwires with length of ~ 0.5 cm and diameter of $30-120\,\mu$m were obtained by suspended melt droplet extraction (SMDE) heated by a high-energy electron beam, followed by rapid cooling at a rate of $\sim 10^6$ K/s [8,15–18]. Initially amorphous microwires (microwire 1, Figure 1, *a*) were subjected to vacuum (10^{-5} Torr) annealing for 2 h at 900° (microwire 2, fig. 1, *b*) during the experiment. The structure looks homogeneous (microwire 1, Figure 1, *a*) before annealing, a chaotic distribution of inclusions is observed after annealing throughout the entire volume of the microwire (microwire 2, Figure 1, *b*).

The samples were analyzed using TESCAN AMBERFIB-SEM scanning electron microscope (FIB — focused ion beam, SEM — scanning electron microscope).

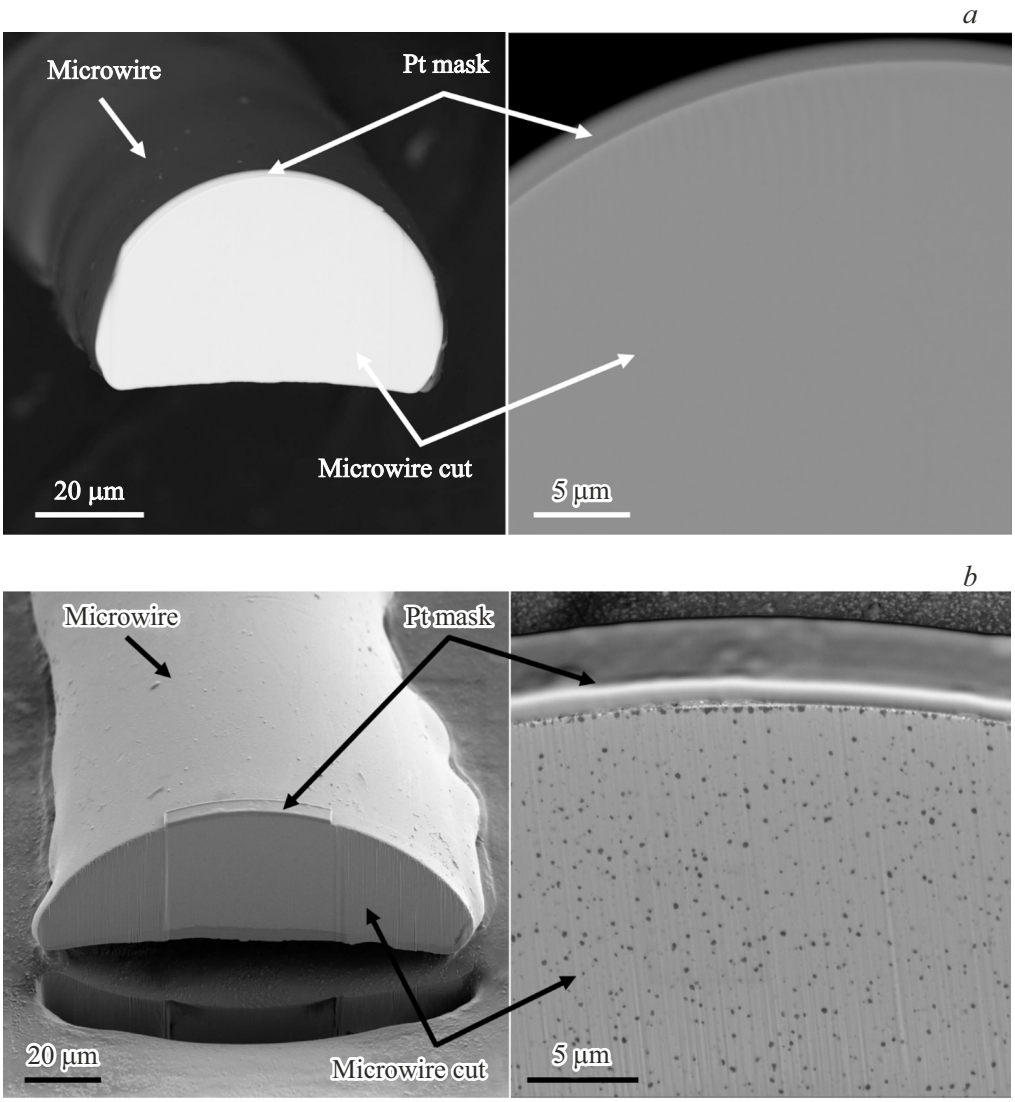

Figure 1. SEM images of microsections of cross-sections of *a*) microwire 1 and *b*) microwire 2.

The ion column makes it possible to prepare micro-sections (Figure 1) and lamellae (Figure 2) of samples in FIB-SEM microscope, using a focused high-energy nanometer beam of positively charged Ga ions, which destroy specified areas of the sample. The vacuum system then pumps out the broken-off parts of the sample. FIB-SEM microscope allows acquiring images of backscattered electrons (BSE). The reflected electronic signal is sensitive to compositional contrast, i. e., sample components of different compositions have different shades of gray in BSE images. This allows visualizing the differences of composition between the components of the sample. FIB-SEM has Oxford Ultim energy dispersion spectrometer and Oxford EBSD detector (EBSD — electron backscattering diffraction).

Thin sections of the surface of microwires 1 and 2 were made using FIB-SEM microscope to study their structure (Figure 1). The thin section is made by irradiation of sample surface with an ion beam incident on it perpendicularly. The analysis of the surface of thin sections makes it possible to determine the structure of the inner layers of the sample, which are inaccessible for the analysis of the surface using classical scanning electron microscopy. A thin section is typically about $15\,\mu$m wide and about $10\,\mu$m deep.

3. Experimental results and discussion

Figures $2, a$ and b show BSE images of cross-sections and maps of the distribution of chemical elements on the cross-section surfaces of microwires 1 and 2, respectively. The BSE images of the surface of the section of microwire 2 show a large number of dark areas that correspond to inclusions of a phase that is different from the main phase (Figure $2, b$). Such features are not observed on the surface of the section of microwire section 1 (Figure $2, a$).

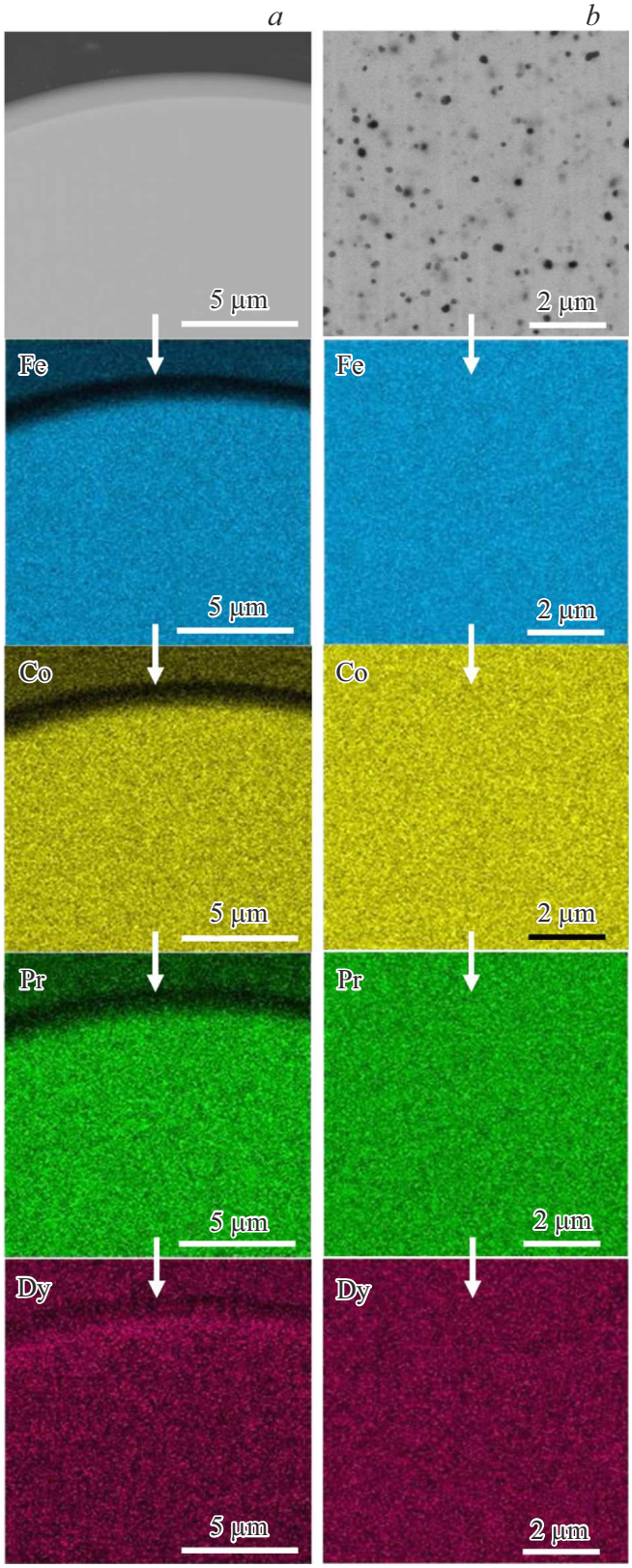

Figure 2. BSE images (gray shapes at the top) of cross-sections of microwires and their corresponding EDX mapping of chemical elements in *a*) microwire 1 and *b*) microwire 2.

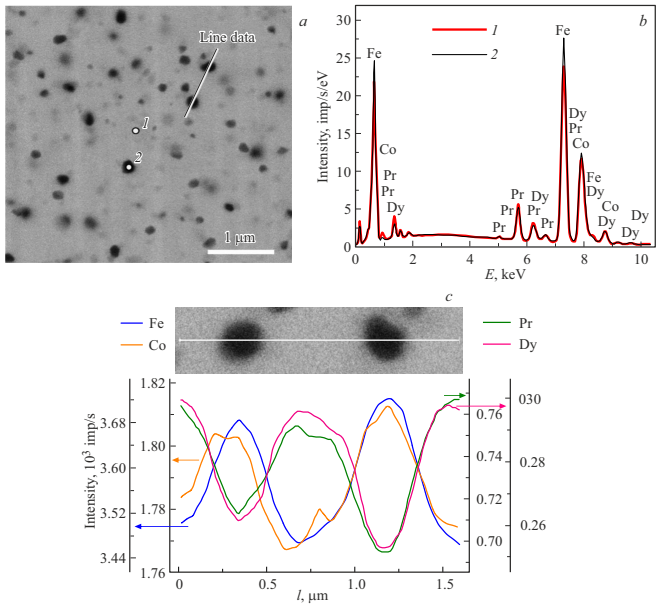

Figure 3. *a*) SEM image and *b*) EDX spectrum in points *1* and *2* of the section of microwire 2. *c*) The distribution of chemical elements along the line in the microwire 2.

The distribution of chemical elements in the ends of microwires 1 and 2 is relatively uniform. Scans of the chemical composition were made along the line shown in the SEM image for analyzing the differences of the chemical composition of the area of the microwire outside the inclusions and the chemical composition of inclusions (Figure 3, *a*). It can be seen that depletion of Dy and Pr atoms and enrichment of Fe and Co atoms are observed in the region of inclusions (Figure 3, *b* and *c*). The areas of inclusions in the BSE images look darker than the surrounding material because they consist of lighter elements.

We performed EDX, SEM and transmission Kikuchi diffraction (TKD) analysis of lamellae made of microwires 1 and 2 to obtain additional information about the structure of the samples. TKD is a method that allows the identification of phases in thin samples (lamellae/foils) with high resolution. The spatial resolution of the X-ray signal for a sample in the form of a thin lamella is noticeably better than in the case of a volumetric sample, since there are no distortions generating an X-ray signal from a large area into the depth of the sample and laterally near the point of incidence of the electron beam.

Images of the freshly prepared lamella in the transmitted electron mode from sensors of bright-field, dark-field and a high-angle dark-field detectors were obtained using a retractable transmitted electron detector (R-STEM) without moving the lamella to another holder. The passed electrons scattered at different angles carry the following information about the studied sample: 1) the bright-field (BF) image conveys the contrast caused by the different electron absorption capacity of the components forming a thin lamella, as well as the Bragg diffraction contrast; 2) the dark-

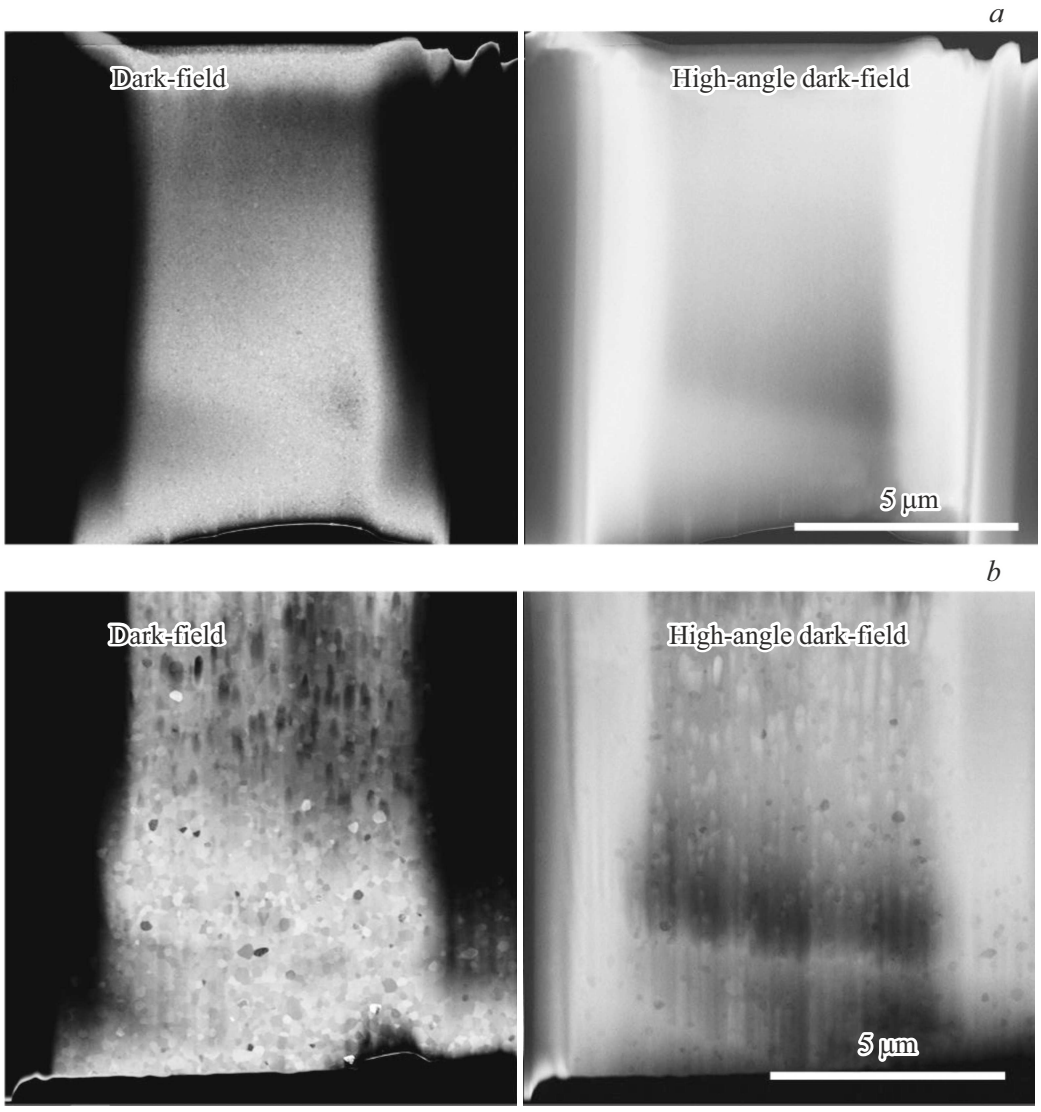

Figure 4. Dark-field (DF) and high-angle-dark-field (HADF) SEM images *a*) of microwire 1 and *b*) microwire 2.

field (DF) image partially contains the orientation contrast characterizing the orientation of inclusions, and partially scattering contrast from light elements; 3) high-angle dark-field (HADF) images characterize the contrast associated with a change in the type of material, with minimal Bragg diffraction contrast. Figure 4 shows DF and HADF images of microwires since the difference between microwires 1 and 2 is strongest in these modes.

Figure 5 shows a diffraction pattern of a microwire before annealing (Figure 5, *a*), which has a halo characteristic of an amorphous alloy, and an diffraction pattern of a microwire after vacuum annealing (Figure 5, *b*), where a large number of point reflexes and the absence of Halos indicate the formation of a polycrystalline structure in amorphous microwires (Figure 5, *b*)

The distribution of chemical elements in the lamellae of microwires 1 and 2 is shown in Figure 6, *a* and *b*, respectively.

The distribution of chemical elements is uniform on the maps of chemical elements obtained for the lamella from microwire 1 (Figure 6, *a*), and a high content of Fe and a reduced content of Pr and Dy is observed in microwire 2 (Figure 6, *b*) in the area of inclusions which is confirmed by X-ray spectral microanalysis of the lamella of microwire 2 (Figure 7). In contrast to the spectrum recorded at point 1, the spectrum recorded at point 2 (inclusion) shows that the content of Fe is higher, and the content of Pr and Dy is lower. Figure 7, *c* shows the distribution of elements along the line indicated in the image as „line data".

TKD analysis is performed using EBSD detector, which records and decodes the Kikuchi pattern (diffraction pattern of reflected/transmitted electrons) from each point on the sample surface when an electron beam from a scanning electron microscope hits this point. Most of the studies described in the literature use TKD to analyze relatively small areas of a sample where the usual EBSD (diffraction

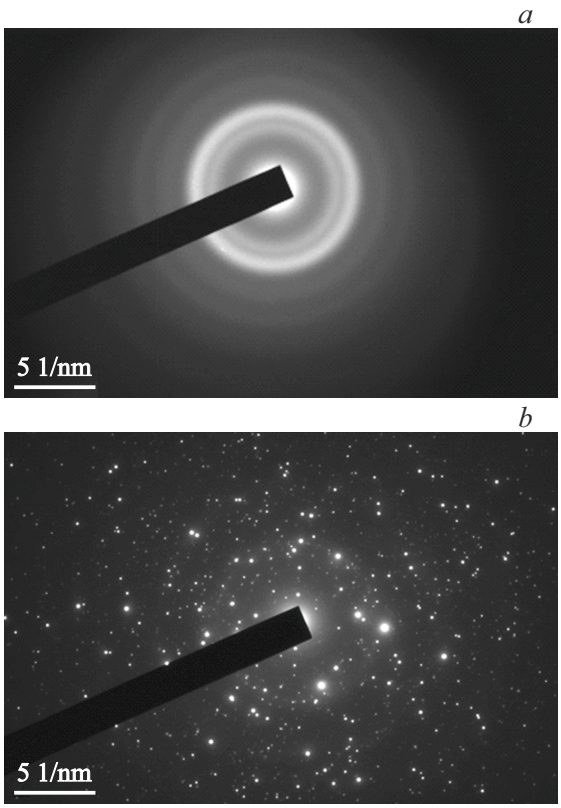

Figure 5. Diffraction patterns for lamellae of amorphous microwire (*a*) and microwire after vacuum annealing (*b*).

pattern of reflected rather than transmitted electrons) cannot provide the required resolution. These samples are usually nanocrystalline metals and alloys.

EDS and EBSD detectors were simultaneously used in FIB-SEM TESCAN AMBER microscope to identify the phases. The EBSD detector allows identifying the crystallographic group of a local area, determining its orientation at each point of the sample surface, and detecting defects and grain boundaries. Kikuchi patterns are recorded using an EBSD detector to identify the phase at selected points, and X-ray spectra are recorded using an EDX detector. Diffraction patterns of reflected electrons were acquired in different regions of the lamella samples before and after annealing. The incident electron beam was directed at an angle of 70° to the horizontal. The image is formed by diffraction of two cone-shaped electron beams when the Wolfe–Bragg condition is fulfilled ($2d \sin\theta = n\lambda$, where d is an interplane distance, θ is an angle between the reflecting plane and the incident beam, λ is a X-ray wavelength, n is a reflection order) for each family of atomic planes. Cone-shaped electron beams were visualized by placing a phosphorescent screen in front of the detector (a highly sensitive camera) on which the cone-shaped electron beams appear as a multitude of thin bands (Kikuchi bands) corresponding to certain families of crystalline planes. The three-dimensional crystallographic orientation

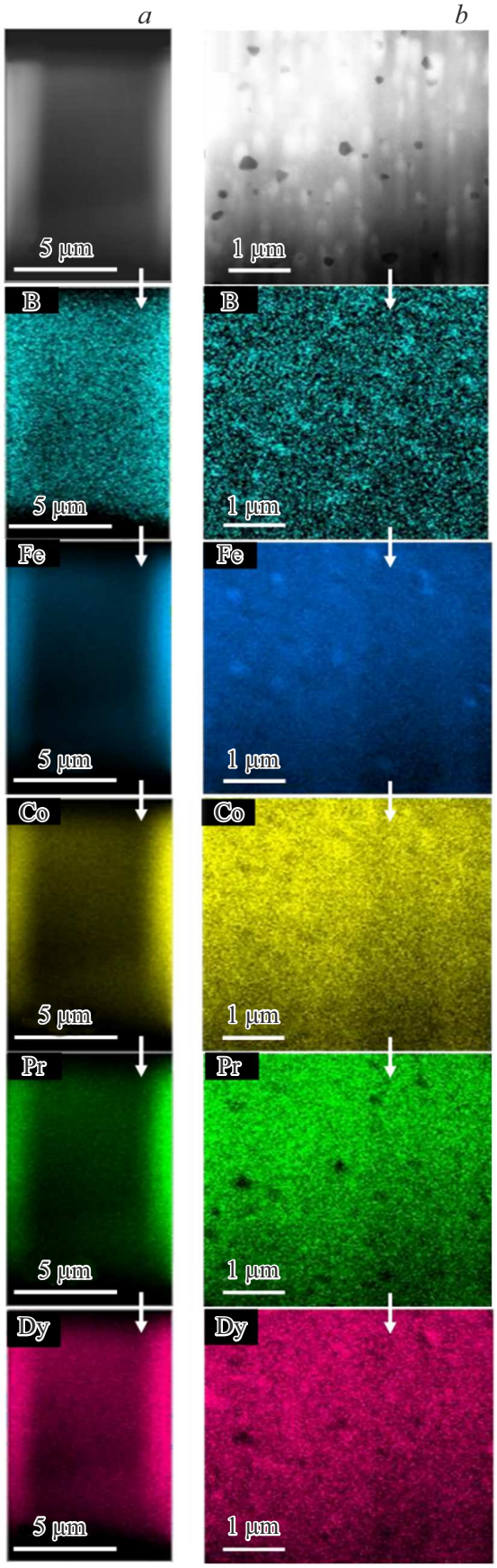

Figure 6. Mapping of chemical elements in lamellae of *a*) microwire 1 and *b*) microwire 2.

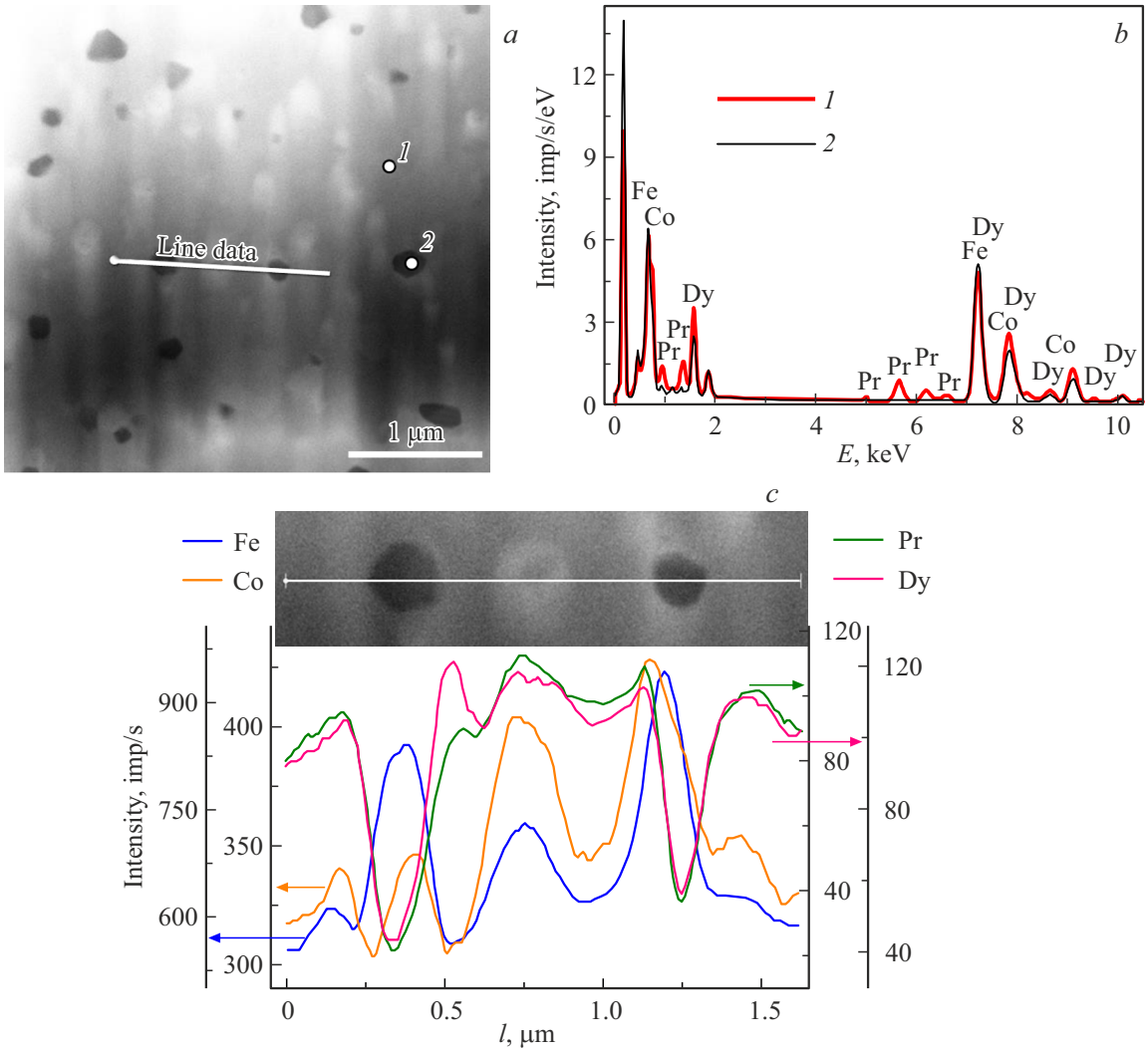

Figure 7. *a*) SEM image of the lamella and *b*) relevant EDX analysis of microwire 2. *c*) The distribution of chemical elements along the line in microwire 2.

of the studied lamella area is determined by the position and relative orientation of the Kikuchi bands automatically using specialized computer programs by comparing the obtained Kikuchi pattern with theoretical data on the corresponding crystalline phase. Then, the phase identification process is carried out based on the chemical composition data and on the basis of crystallographic data. The presence of bands, the angles of their mutual intersection and the width of the bands depend on the observed spatial group of the crystal structure and the orientation of the crystal structure. A small section of the lamella of annealed microwire 2 was used to obtain several Kikuchi patterns recorded in the areas of inclusions (points $X1$, $X2$) and several Kikuchi patterns outside the inclusions (points $Y1$, $Y2$) (Figure 8).

The lattice structure is defined as a body-centered cubic (BCC) at points $X1$ and $X2$. There may be cobalt atoms in the nodes of this lattice in addition to iron atoms. The lattice structure is defined as tetragonal $Pr_2Fe_{14}B_1$ 2-14-1 at points $Y1$ and $Y2$. It is possible that some of the praseodymium atoms in this lattice are replaced by dysprosium atoms. The lattice cell parameters were obtained using the built-in HKL phases databases (HKL) (J. Appl. Phys. [JAPIAU], vol. 42, pages 4290–4295) and the Inorganicrystalline Structure Database (ICSD) (J. Appl. Phys. [JAPIAU], (1985) vol. 57, pages 2343–2345).

The occurrence of inclusions with a depleted composition of rare earth metals is obviously limited by diffusion processes during annealing. The occurrence of such inhomogeneities with cubic symmetry in a tetragonal structure is energetically unfavourable. This indicates that the nonequilibrium amorphous state in the initial state of the microwire generates new thermodynamically nonequilibrium states in case of rapid conversion to the crystalline phase. It is known that the excess Gibbs free energy does not relax to the lowest energy state (tetragonal phase), but leads to the generation of intermediate metastable states (inclusions). The depletion of clusters (inclusions) by rare-earth atoms can be explained by the fact that their diffusion mobility is

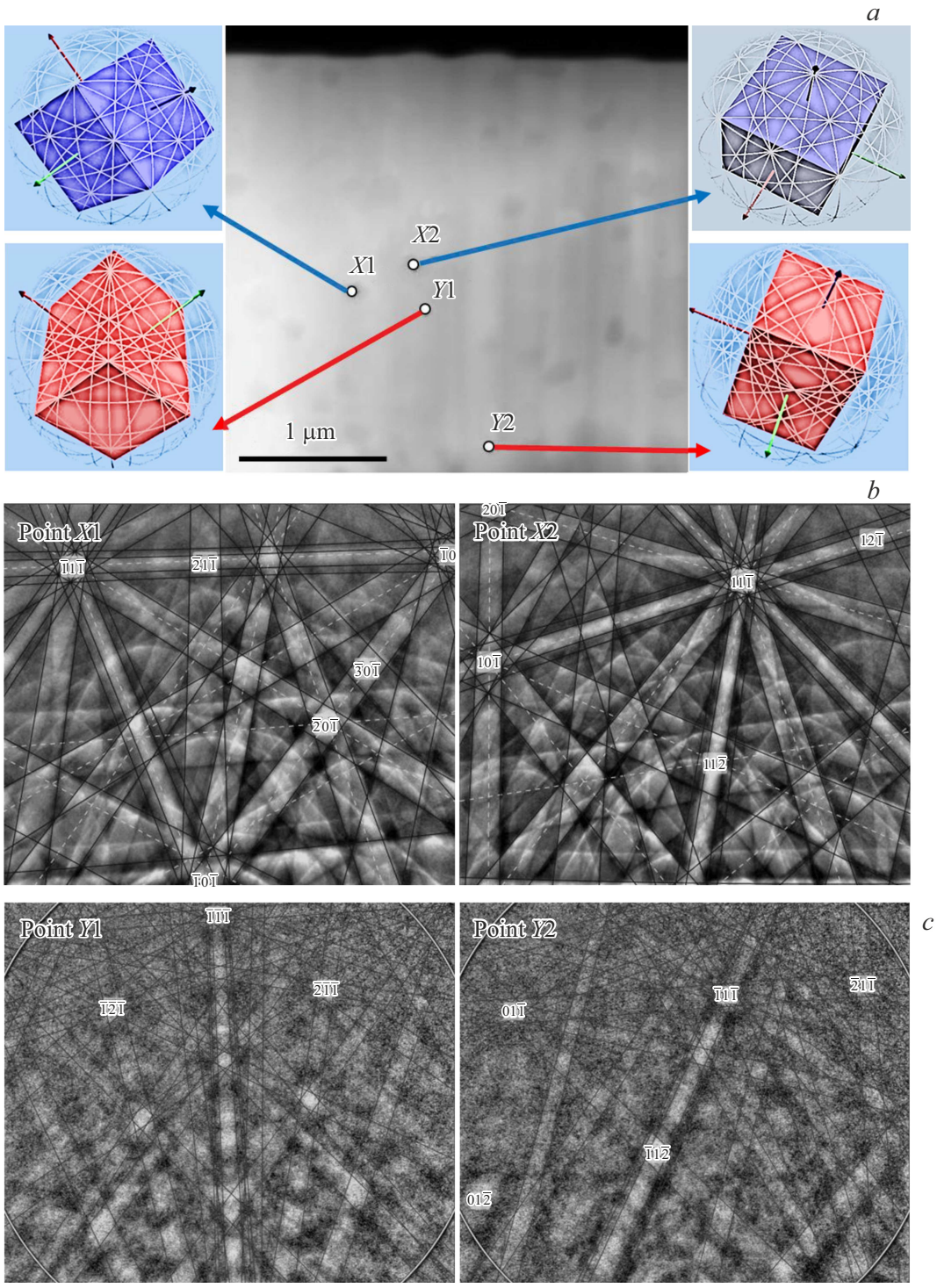

Figure 8. *a*) SEM image of microwire 2 with indicated points at which Kikuchi patterns and their corresponding crystal phase orientations were recorded. *b*) Kikuchi patterns obtained in the area of inclusions — points $X1$ and $X2$. *c*) Kikuchi patterns obtained outside the area of inclusions — points $Y1$ and $Y2$.

significantly (by two orders of magnitude) lower than the diffusion mobility of transition metal atoms.

We would like to also note that according to Ref. [18] the magnetic properties of the annealed microwire, although approaching the expected properties of the magnetically rigid phase 2-14-1, still turn out to be different than in this phase. This is explained both by the presence of inclusions that occupy a significant volume fraction of the microwire ($\sim$ 10%), and by the influence of these inclusions on the domain structure and remagnetization of the sample in a

magnetic field. Thus, the specificity of micromagnets is related to the presence of nonequilibrium inclusions in them.

4. Conclusion

In an initially amorphous microwire, vacuum annealing leads to the formation of inclusions with a high content of iron and cobalt and a low content of praseodymium and dysprosium. After annealing, the lamellae contain $\sim 10\%$ of inclusions with a body-centered crystal lattice with a lack of rare-earth atoms. The crystal structure becomes tetragonal 2-14-1 outside the inclusions after annealing. Microwires with inclusions represent a nonequilibrium metastable or labile medium. Inclusions occur as a result of self-organization of the material under conditions of strong disequilibrium of the initial amorphous state.

Funding

The study was carried out within the framework of the state assignment of the Federal Research Center for Problems of Chemical Physics and Medical Chemistry of the Russian Academy of Sciences 124020700089-3.

Conflict of interest

The authors declare that they have no conflict of interest.

References

[1] A. Khosla, S. Kassegne. Microsyst. Technol. **21**, *11*, 2315 (2015).
[2] H. Li, T.J. Flynn, J.C. Nation, J. Kershaw, L. Scott Stephens, C.A. Trinkle. J. Micromech. Microeng. **23**, *6*, 065002 (2013).
[3] J. Töpfer, V. Christoph. Sens. Actuator A: Phys. **113**, *2*, 257 (2004).
[4] N. Wang, B.J. Bowers, D.P. Arnold. J. Appl. Phys. **103**, *7*, 07E109 (2008).
[5] A. Walther, C. Marcoux, B. Desloges, R. Grechishkin, D. Givord, N.M. Dempsey. J. Magn. Magn. Mater. **321**, *6*, 590 (2009).
[6] P. Corte-León, J.M. Blanco, V. Zhukova, M. Ipatov, J. Gonzlez, M. Churyukanova, S. Taskaev, A. Zhukov. Sci. Rep. **9**, *1*, 12427 (2019).
[7] K.-W. Moon, D.-H. Kim, C. Kim, D.-Y. Kim, S.-B. Choe, C. Hwang. J. Phys. D **50**, *12*, 125003 (2017).
[8] O.V. Koplak, E.V. Dvoretskaya, V.L. Sidorov, N.N. Dremova, I.V. Shashkov, D.V. Korolev, R.A. Valeev, V.P. Piskorski, R.B. Morgunov. J. Surf. Invest.: X-Ray, Synchrotron Neutron Tech. **15**, *2*, 292 (2021).
[9] V. Vieille, R. Pétrot, O. Stéphan, G. Delattre, F. Marchi, M. Verdier, O. Cugat, T. Devillers. Adv. Mater. Technol. **5**, *10*, 2000535 (2020).
[10] J. Alam, A.Kh.Kh. Zedan, M.G. Nematov, N.A. Yudanov, A.S. Kurochka, A.V. Nuriev, L.V. Panina, V.G. Kostishin. Phys. Met. Metallogr. **124**, *1*, 1 (2023).
[11] J. Nabias, A. Asfour, J.-P. Yonnet. IEEE Trans. Magn. **53**, *4*, 4001005 (2017).
[12] M. Malátek, P. Ripka, L. Kraus. Sens. Actuator A: Phys. **147**, *2*, 415 (2008).
[13] A.A. Fuks, G.E. Abrosimova, O.I. Aksenov, A.S. Aronin. Phys. Solid State **65**, *1*, 34 (2023).
[14] M. Takezawa, Y. Harada, Y. Honkura, S. Honkura. Sensors **23**, *7*, 3506 (2023).
[15] O.V. Koplak, V.L. Sidorov, E.V. Dvoretskaya, I.V. Shashkov, R.A. Valeev, D.V. Korolev, R.B. Morgunov. Phys. Solid State **63**, *2*, 266 (2021).
[16] O.V. Koplak, E.V. Dvoretskaya, D.V. Korolev, R.A. Valeev, V.P. Piskorskii, M.V. Gapanovich, Yu.S. Pogorelets, R.B. Morgunov. Phys. Solid State **63**, *10*, 1675 (2021).
[17] O.V. Koplak, E.V. Dvoretskaya, D.V. Korolev, R.A. Valeev, V.P. Piskorskii, A.S. Denisova, R.B. Morgunov. Phys. Solid State **62**, *8*, 1333 (2020).
[18] E.V. Dvoretskaya, R.B. Morgunov, A.I. Chernov. Mater. Lett. **377**, 137408 (2024).
[19] D.V. Korolev, V.P. Piskorskii, R.A. Valeev, O.V. Koplak, R.B. Morgunov. Phys. Solid State **63**, *8*, 1218 (2021).

Translated by A.Akhtyamov